Mechanisms for the Generation of Mesoscale Vorticity Features in Tropical Cyclone Rainbands

CHARMAINE N. FRANKLIN

Department of Mathematics and Statistics, RMIT University, Melbourne, Victoria, Australia

GREG J. HOLLAND

Aerosonde Robotic Aircraft, Notting Hill, Victoria, Australia

PETER T. MAY

Bureau of Meteorology Research Centre, Melbourne, Victoria, Australia

(Manuscript received 12 July 2004, in final form 19 January 2006)

ABSTRACT

A high-resolution tropical cyclone model with explicit cloud microphysics has been used to investigate the dynamics and energetics of tropical cyclone rainbands. Analysis of the vorticity interactions that occur within the simulated rainbands demonstrates that couplets of cyclonic–anticyclonic mesovortices can be produced in outer bands. The primary source of this vorticity is the upward tilting of system-generated horizontal vorticity by diabatic heating gradients. The vertical heating gradient in the stratiform cloud also creates a potential vorticity (PV) dipole that accelerates the tangential flow and develops a midlevel jet. The strength of the jet is enhanced by the vortex pair that is oriented radially across the rainband. The Fourier decomposition of the absolute vorticity field shows two counterpropagating vortex Rossby waves associated with the rainband. The wave located on the inner side of the band transports energy toward the vortex center. The outer wave is made up of high wavenumbers and uses the vorticity gradients generated by the rainband. The results support the hypothesis that the heating profile in the stratiform regions of rainbands generates cyclonic PV across the freezing level, which develops a midlevel jet. This mechanism creates a vorticity gradient that enables the propagation of vortex Rossby waves that could allow the rainbands to interact with the mean flow and potentially influence the evolution of the storm by contributing to the symmetric component of vorticity and the development of secondary eyewalls.

1. Introduction

The dynamics of tropical cyclone rainbands are not completely understood. They have characteristics that hint at processes that both intensify (e.g., May and Holland 1999) and limit tropical cyclones (e.g., Powell 1990b). Tropical cyclone rainbands are generally characterized by extensive regions of stratiform precipitation with embedded convective elements showing varied degrees of organization (e.g., Barnes et al. 1991; May 1996). Observations of these bands often show a midlevel jet (Willoughby et al. 1984; Jorgensen 1984; Marks 1985; May et al. 1994; Samsury and Zipser 1995) and an associated local vorticity maximum. Vertical velocity profiles in the stratiform precipitation regime are of a mesoscale updraft above the melting level and a mesoscale downdraft below, similar to observations of the trailing anvils of deep tropical convection (e.g., Gamache and Houze 1982; May and Rajopadhyaya 1996). May et al. (1994) proposed that the heating profile in the stratiform regions could provide a mechanism for the production of potential vorticity (PV; Raymond and Jiang 1990), which may in turn be responsible for the development of the midlevel jet and be a source of high-PV air in the core. May and Holland (1999) demonstrated that PV production in the stratiform region of rainbands could develop the observed vorticity and

---

Corresponding author address: Charmaine Franklin, Bureau of Meteorology Research Centre, GPO Box 1289K, Melbourne, VIC 3001, Australia.
E-mail: c.franklin@bom.gov.au

wind maxima, although their data were too limited for definite conclusions.

The production of PV in rainbands can generate a mechanism through which the asymmetric bands can interact with the mean flow by perturbing the basic-state PV field and enabling the propagation of vortex Rossby waves. For example, Smith and Montgomery (1995) showed that at larger radii such as those for outer rainbands, higher azimuthal wavenumber disturbances are confined to these radii due to the damping of the perturbation by strong shear in the process of axisymmetrization. Therefore, asymmetric vorticity generated in rainbands can positively influence the intensification of the storm by contributing to the symmetric component of vorticity. Vorticity generated in the rainbands may also affect the intensification cycle of the tropical cyclone through the development of secondary eyewalls and eyewall replacement (Willoughby et al. 1982). Möller and Montgomery (2000) showed that PV asymmetries outside of the radius of maximum winds acted to intensify the outer tangential winds through wave-mean flow and wave–wave interactions. Their results demonstrated that the change in the primary circulations induced a secondary circulation that resulted in subsidence near the radius of maximum winds, which could weaken the eyewall.

Most of the published results investigating the theory of PV asymmetries and vortex Rossby waves in tropical cyclone vortices have used idealized models (e.g., Montgomery and Enagonio 1998; Möller and Montgomery 1999, 2000). Other full-physics modeling studies have focused on inner rainbands and eyewall dynamics (Chen and Yau 2001; Wang 2001, 2002); however, in this study we focus on the vorticity asymmetries produced by outer rainband dynamics. This study will test the hypothesis that PV generated in the rainbands can develop a midlevel jet by using a full-physics model within an idealized domain, where there is no interaction with other weather systems or complexities introduced from features such as topography or sea surface temperature variations. Specifically, we will examine the growth of a vortex pair within a rainband and the relationship between the vorticity couplet and the midlevel jet. Both of these features are generated by the diabatic forcing of the stratiform regions of the rainbands and we will demonstrate that without the cooling from evaporation, neither a distinct jet nor a vortex pair is generated. We will show how the development of the jet is related to the PV field in the stratiform precipitation regions in the bands, and will demonstrate the stability of the anticyclonic gyre of the vortex pair and the response of the vortex pair as a vortex Rossby wave.

2. Numerical model description

The numerical simulations in this study were performed with the TCM3 model described by Wang (1999). This model is a three-dimensional hydrostatic, triply nested moveable mesh tropical cyclone model. The model is formulated with Cartesian coordinates in the horizontal and 20 sigma levels in the vertical, with higher resolution in the boundary layer. The governing equations are solved on the Arakawa A grid. The spatial discretization uses second-order-conservative finite differences, while the second-order leapfrog scheme is utilized for the time integration. The model physics include an E–ε turbulence closure scheme, a modified Monin–Obukhov scheme, and an explicit microphysics parameterization that predicts six water categories. The resolutions of the three meshes are 45, 15, and 5 km, with corresponding timesteps of 450, 150, and 50 s, respectively. The model environment was initialized with the January mean relative humidity and environmental soundings for Willis Island, northeast of Australia (Holland 1997), and the sea surface temperature is fixed at 29°C. Initially the vortex is positioned at 18°S and has a maximum tangential wind of 25 $\mathrm{m\,s^{-1}}$ at a radius of 100 km. The storm is simulated in an environment at rest on a β plane, which includes the variation of the Coriolis force with latitude.

In the inner region of tropical cyclones the radius of curvature is tight and using Cartesian coordinates can introduce errors. Hence in section 3, vorticity and divergence fields are calculated in cylindrical coordinates, which eliminates an erroneous wavenumber 2 feature that occurs with the Cartesian analysis in the area bounded by the 50-km radius. For ease of interpretation, cyclonic vorticity is denoted as positive even though the storm is a Southern Hemisphere cyclone. Extending this notation to the budgets, positive (negative) values denote an increase (decrease) in the cyclonic vorticity. A detailed description of the model and the initialization procedure is given in a companion paper (Franklin et al. 2005); this paper also compares the simulated rainband characteristics with observations and documents the sensitivity of the bands to microphysical parameters.

3. Rainband structure

The model is spun up from prescribed initial wind fields. Principal-type rainbands develop at about 48 h into the run and throughout the remainder of the simulation the presence of cyclonic–anticyclonic vorticity couplets appears in several rainbands. This vorticity structure of a couplet radially across the rainband, with

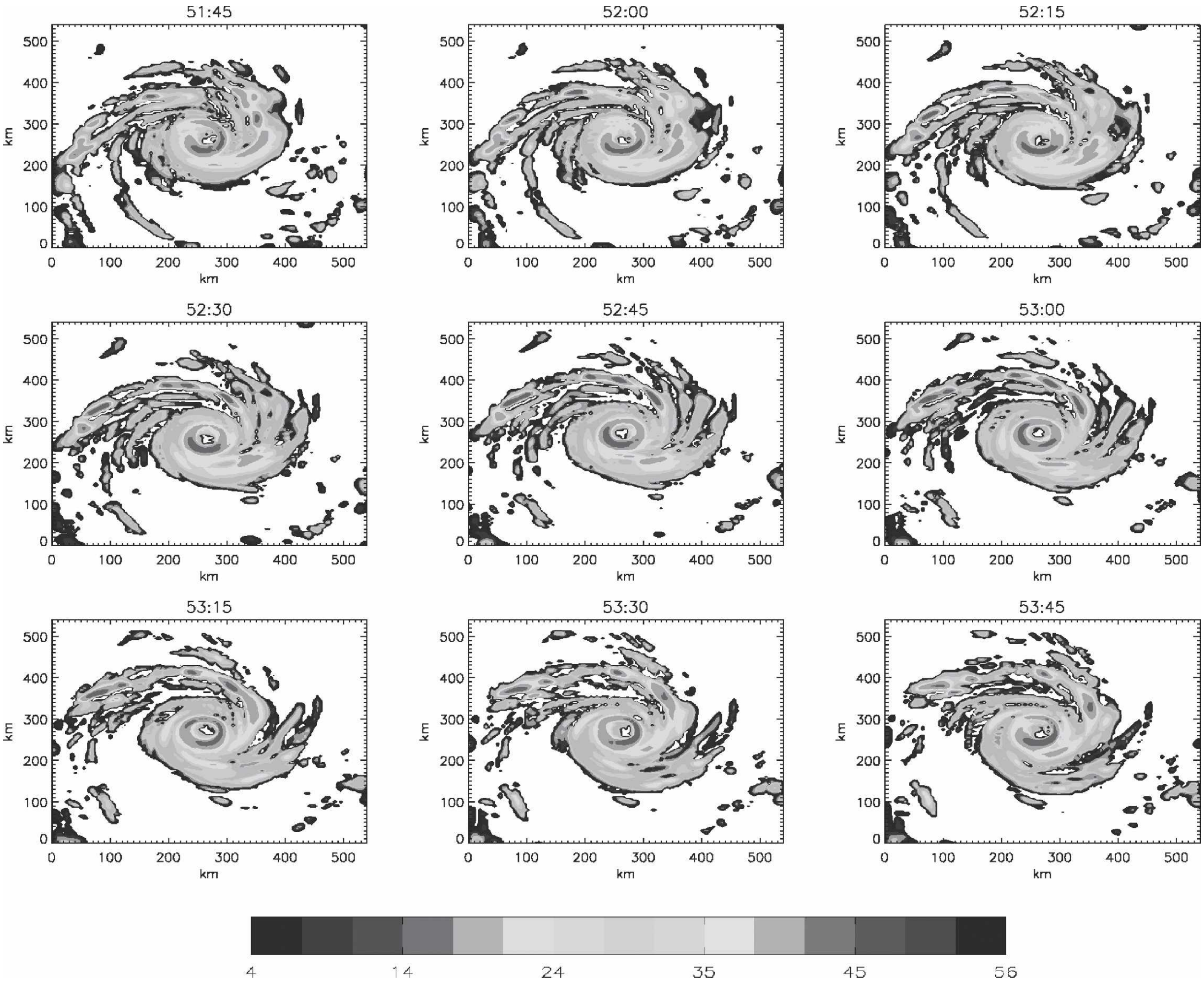

FIG. 1. Surface pseudo-radar-reflectivity fields (dBZ) for a beta-plane simulation. The panels are for the times 51 h 45 min–53 h 45 min in increments of 15 min. The domain shown in each panel is 540 km × 540 km.

the anticyclonic region located on the outer side of the band, is a common feature in this simulation. We choose to focus on one particular case to examine, in detail, the mechanisms for the generation of these vorticity features.

Figure 1 shows the simulated reflectivity fields at the surface for the times from 51 h 45 min to 53 h 45 min. The rainband of interest, which displays the typical band structure in the simulation, is initially located on the eastern side of the storm. At 51 h 45 min the band displays surface reflectivities greater than 40 dBZ, with the highest reflectivities rivaling those in the eyewall. Over the next 45 min the convection dissipates and moves downwind leaving a region of weak reflectivities, with maximum values of about 35 dBZ in the trailing section of the band. From 52 h 30 min until 53 h 30 min the higher-reflectivity region embedded within the largely stratiform area moves to the inner side of the band and rotates inward to where the band and the eyewall meet. After this time, the rainfall becomes less intense and the band begins to lose its spiral structure. A new band that has been developing north of the vortex center moves in to replace the remnants of this decaying band.

Vorticity analysis

Outside the radius of maximum winds, tropical cyclone rainbands are generally characterized by weak cyclonic relative vorticity in the mid- to low levels, despite the strong cyclonic circulation (e.g., Frank 1977; May et al. 1994). Examination of the absolute vorticity field (Fig. 2) shows a region of anticyclonic (denoted as negative values) absolute vorticity occurring in the rainbands at the 600–800-hPa level. This means that regions

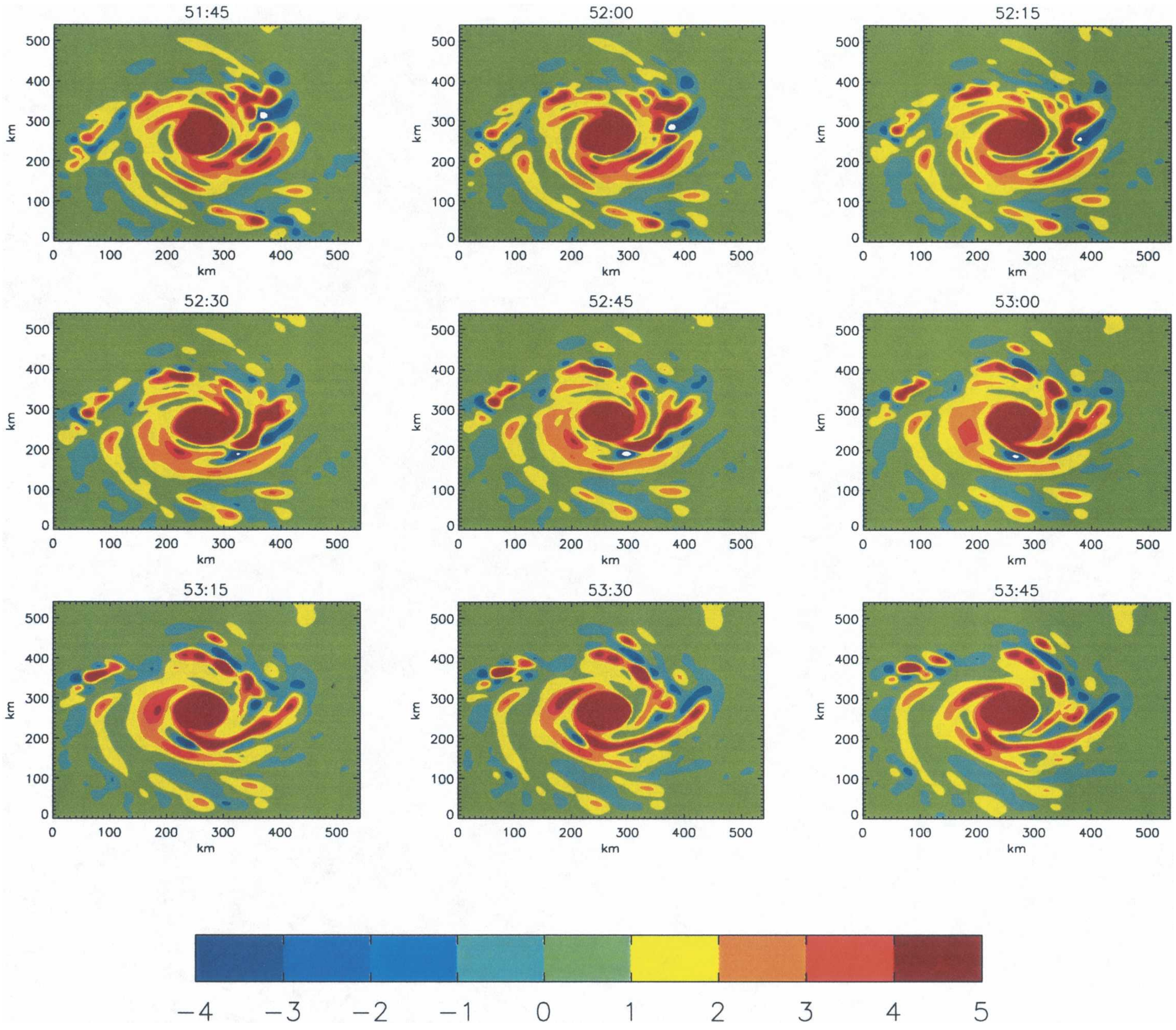

FIG. 2. Vertical component of absolute vorticity ($\times 10^{-4}$ s^{-1}) at the 695-hPa level. The white regions represent values $<-4 \times 10^{-4}$ s^{-1}, while values $\geq 4 \times 10^{-4}$ s^{-1} are indicated by the darkest color.

of air below the freezing level are inertially unstable (e.g., Hoskins 1974; Emanuel 1983). The regions of inertial instability are a consistent feature within the model-simulated rainband, both in location and time, and they are coupled with regions of cyclonic vorticity. The following work investigates the mechanisms responsible for the generation and maintenance of the cyclonic–anticyclonic vorticity couplet and the relationship between this region and the midlevel jet.

1) ORGANIZATION AND EVOLUTION

The panels of absolute vorticity for the 695-hPa level in Fig. 2 show two anticyclonic regions in the rainband at 51 h 45 min. The area of maximum anticyclonic vorticity is located on the outer upwind section of the band. It is about 40 km long in the azimuthal direction and is less than -5.5×10^{-4} s^{-1}, or an order of magnitude larger than the Coriolis force at this latitude. This anticyclonic mesovortex lies radially adjacent to a cyclonic mesovortex that is weaker in magnitude. The other region of anticyclonic vorticity is farther downwind on the mid-inner side of the band. It is less intense, -3.1×10^{-4} s^{-1}, and has been stretched in the azimuthal direction. Over time these two areas of anticyclonic vorticity move slowly downwind along the band, as well as being rotated around the eyewall with the band. Initially the upwind anomaly appears to be disrupting the azimuthal structure of the band, and then it is strained by the radial shear of the azimuthal wind of the vortex and becomes more of an anticyclonic vortex filament

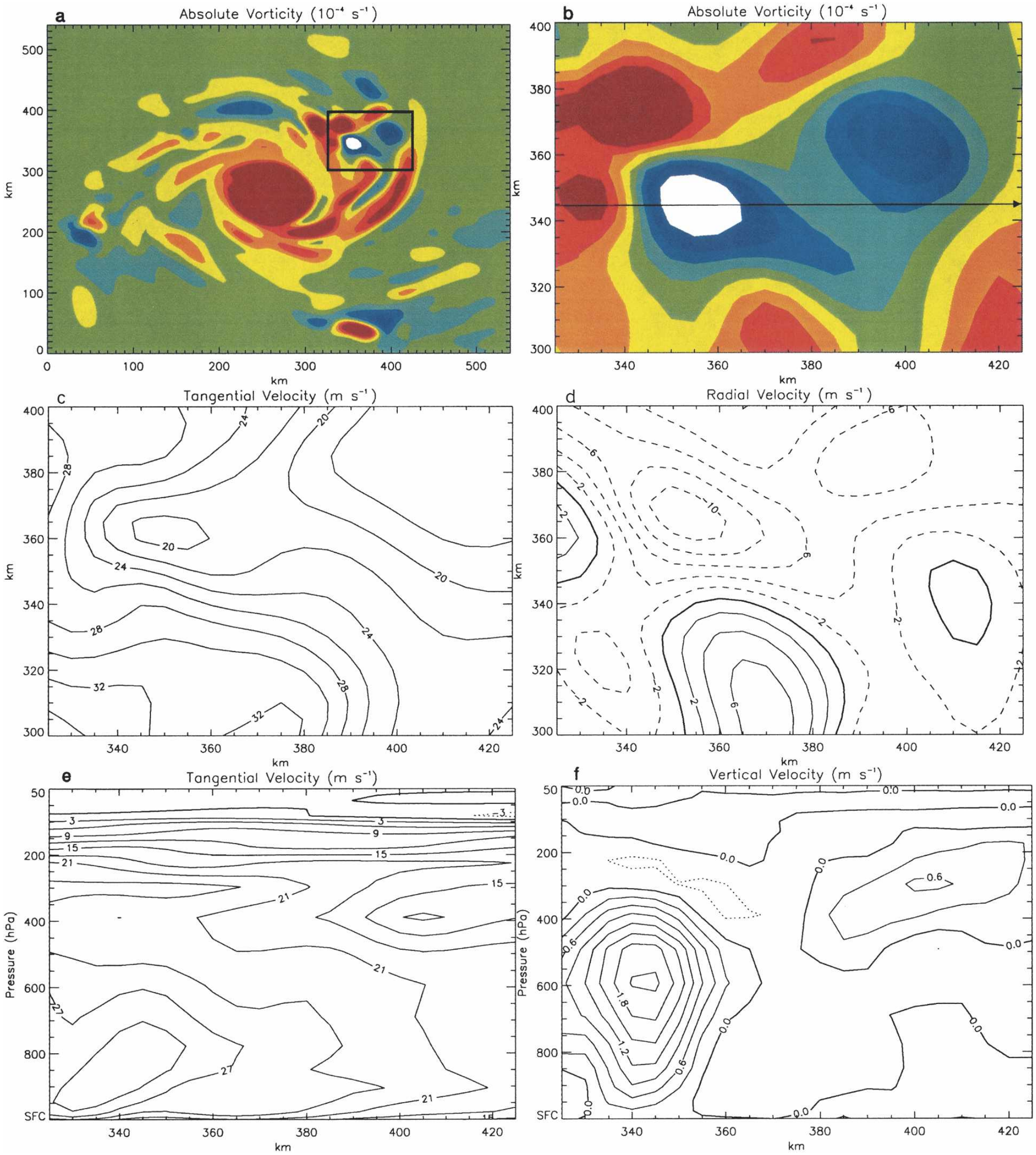

FIG. 3. (a) Plan view of the absolute vorticity at the 600-hPa level at 51 h 30 min, contoured as per Fig. 2, (b) the boxed region of (a), (c) tangential velocity (contour interval 2 m s^{-1}), (d) radial velocity (contour interval 2 m s^{-1}), (e) tangential velocity along the section depicted in (b) (contour interval 3 m s^{-1}), and (f) vertical velocity (contour interval 0.3 m s^{-1}).

on the outer boundary of the band. It reduces in size and intensity, and remains located on the outer flanks of the band until it is dissipated along with the rainband. From 52 h 15 min to 52 h 45 min the downwind region of anticyclonic vorticity strengthens and is advected closer to the center of the storm. The anticyclonic vorticity associated with the rainband then weakens as the band decays.

The cyclonic–anticyclonic vorticity couplet on the outer upwind section of the band is stronger at the 600-hPa level compared with the 695-hPa level, with the anticyclonic vorticity increasing by -1.3×10^{-4} s^{-1} over almost 100 hPa, and is located farther upwind. Figure 3 shows the air motions within this area at 51 h 30 min at 600 hPa. Figure 3d shows that the region of maximum anticyclonic vorticity has a dipole of radial inflow and outflow, whose shear is twice that of the azimuthal flow's shear (Fig. 3c). The radial flow dipole is associated with a minimum in the tangential winds.

Figure 4 shows how the tilting of horizontal vortex

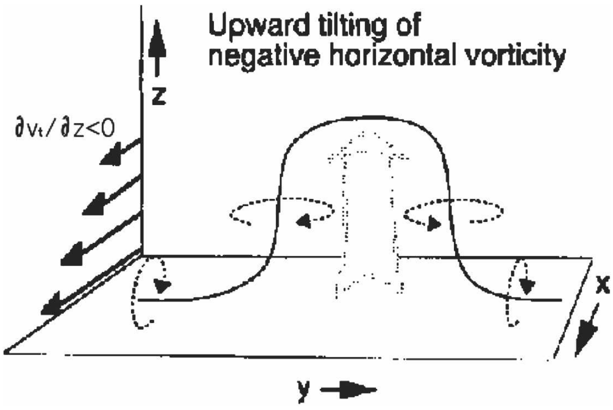

FIG. 4. Schematic of vertical vorticity generation through vortex tilting, where *x* represents the tangential direction and *y* the radial. Upward motion pushes the vortex lines up in the center, producing cyclonic rotation on the inner side and anticyclonic on the outer. [Modified from Pandya et al. (2000), adapted from Weisman and Davis (1998).]

lines into the vertical can generate vertical vorticity. A cyclonic–anticyclonic vorticity couplet develops radially across the band (see Fig. 3a), with an updraft core located in between the pair (Figs. 3b and 3f). The vorticity couplet in the rainband is a result of a convective updraft tilting the radial vortex lines into the vertical. It is the tangential wind shear (see Fig. 3e) that is responsible for the radial vortex lines, which is inherently due to the warm-core structure of the cyclone as well as the diabatic processes in the stratiform regions that give rise to the maximum of the tangential winds occurring in the midlevels. The generation of radial vorticity in the stratiform region, which is characterized by heating above the melting level and cooling below due to evaporation and melting, continues through the diabatically induced convergence of the vertical velocity in the midlevels (e.g., Weisman 1992). These radial vortex lines are present in the rainband prior to when we see the development of the vorticity couplet. The tangential wind maximum at 51 h 30 min is located at about 850 hPa (Fig. 3e) and this is represented as the lowest level in Fig. 4. The vertical profile of absolute vorticity shows that the vorticity couplet exists predominately above this level (not shown), which is consistent with the schematic. Figure 4 shows how the vertical shearing of the azimuthal flow combined with the vertical motion is the principle mechanism responsible for the formation of the vorticity couplet. The pair of mesocyclones is associated with the upward motion of a convective cell moving downwind through the stratiform region of the band. As the updraft moves through the stratiform region of the band, these radial vortex lines are tilted into the vertical resulting in the observed vorticity couplet.

The structure of the vorticity couplet is dynamically similar to the line-end vortices observed behind the convective lines of squall systems (e.g., Jorgensen et al. 1997). Numerical simulations of these mesoscale convective vortex pairs have demonstrated that they may form as a result of the tilting of system-generated or environmental horizontal vorticity (e.g., Weisman and Davis 1998). Our numerical simulations are performed in idealized environments to enable us to investigate the underlying physics, with the view to extend the knowledge of tropical cyclone rainband dynamics and energetics. This means that the mesovortices here arise from internal processes. It has been suggested that mesovortices in squall lines can affect the strength of rear-inflow jets and may play a role in initiating new convective elements (e.g., Weisman 1992) and thus could be an important element in the evolution of tropical cyclones.

2) VORTICITY BUDGET

The region of anticyclonic vorticity is persistent in location and time. To investigate what mechanisms maintain it against the strong, inertially stable flow of the storm core, the vorticity budget has been calculated. Ignoring friction and the Rossby parameter, the vertical component of the vorticity equation in cylindrical-sigma coordinates is given by

$$\frac{d\zeta_a}{dt} = -\zeta_a\left(\frac{v_r}{r} + \frac{\partial v_r}{\partial r} + \frac{1}{r}\frac{\partial v_t}{\partial \lambda}\right) + \left(\frac{1}{r}\frac{\partial \dot{\sigma}}{\partial \lambda}\frac{\partial v_r}{\partial \sigma} - \frac{\partial \dot{\sigma}}{\partial r}\frac{\partial v_t}{\partial \sigma}\right). \tag{1}$$

The left side of (1) represents the local tendency of ζ_a plus the transport due to the horizontal and vertical winds. The first term on the right side of the equation is the stretching term, which represents the generation of vorticity by horizontal divergence. Divergence (convergence) is associated with an increase (decrease) in area and given the conservation of angular momentum, this implies a decrease (increase) in vorticity (Holton 1992). The second term on the right is the tilting or twisting term. This term represents the vertical vorticity generated by the tilting of horizontally oriented components of vorticity into the vertical, as shown in Fig. 4.

The advection term of the absolute vorticity budget is large and is balanced predominately by the local tendency because of the region of anticyclonic vorticity being advected along the band (see Fig. 2). The generation and maintenance of the anticyclonic mesovortex occurs by the divergence and tilting terms. The divergence and tilting terms at the 695-hPa height at 51 h 45 min are shown in Fig. 5. The newly formed outer, upwind region of anticyclonic vorticity is generated

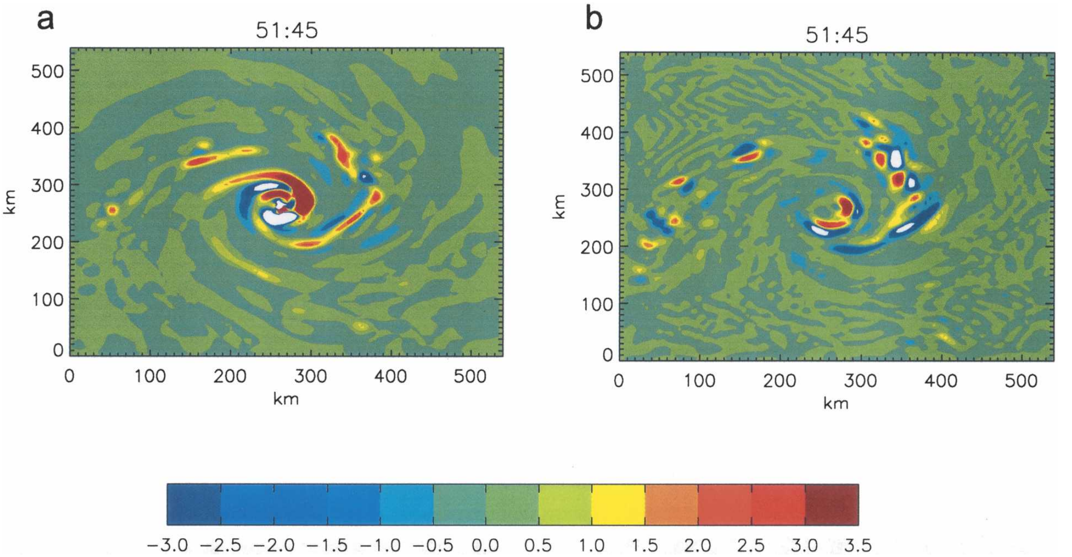

FIG. 5. (a) Divergence and (b) tilting term of the vorticity equation ($\times 10^{-7}$ s^{-2}) at the 695-hPa level, where positive (negative) values denote an increase (decrease) of cyclonic vorticity.

mostly by the tilting term but there is a significant contribution at this time from the divergence term. The position of the anticyclonic mesovortex is clearly identifiable by the region of anticyclonic vorticity generation in Fig. 5a, which is greater than -3.0×10^{-7} s^{-2}. Because there is existing anticyclonic flow that is substantial compared with the cyclonic earth term, stretching can produce an increase of anticyclonic vorticity. Examination of the tilting term at 51h 45 min shows that the upwind end of the band is composed of a series of cyclonic–anticyclonic generation pairs, with the magnitude of the vorticity in the couplet of interest exceeding -3.0×10^{-7} s^{-2}. Over time the divergence term maintains the outer instability and the tilting term removes the anticyclonic vorticity by creating cyclonic vorticity. From 53 h 00 min the outer anticyclonic vorticity from this time is not maintained by either mechanism and the inner region has a small anticyclonic contribution by the divergence term. Over the next 30 min the anticyclonic fluid is strained and wrapped into the vortex.

3) RELATIONSHIP TO THE MIDLEVEL JET

Plan views of tangential velocity at the 600-hPa level are shown in Fig. 6. A well-defined jet in the rainband is apparent at this level from 52 h 30 min to 53 h 00 min. Comparison with Fig. 2 shows that the radial location of the jet lies in the region between the cyclonic–anticyclonic vorticity couplet. In our case the jet and associated dynamics are comparable to squall-line modeling studies (e.g., Lafore and Moncrieff 1989; Weisman 1992) and observations (Smull and Houze 1987). These numerical simulations show that rear-inflow jets develop as the squall line matures into a more stratiform structure. This is in part due to the cold pool that is produced by the melting and evaporation below the base of the anvil cloud, which is responsible for the buoyancy gradients that generate the horizontal vorticity in the mid- to low levels (Rotunno et al. 1988). The region of heating and positive buoyancy above the cloud base works in conjunction with the cooling below to accelerate the rear-to-front flow at the midlevels (Lafore and Moncrieff 1989). These gradually descending midlevel flows were observed by Kingsmill and Houze (1999) to originate at a height between 5 and 10 km and descended to about 3 km, with a few cases extending to the surface. Braun and Houze (1997) demonstrated the role of sublimative cooling below the stratiform cloud base as a physical mechanism involved in the initiation of the rear-inflow core above the melting level.

The jet in our simulations is only developed after the band displays a predominantly stratiform structure. The vertical heating profile in the stratiform precipitation region creates a zone of convergence and accelerates the flow in the midlevels. The development of the jet by diabatic forcing is explored further in section 4 using PV dynamics. The strength of the jet is enhanced by the vorticity couplet that is developed independently of the jet when a convective updraft moves downwind through the band, tilting the horizontal vorticity lines into the vertical as discussed previously. The diabatic forcing that creates convergence in the midlevels is re-

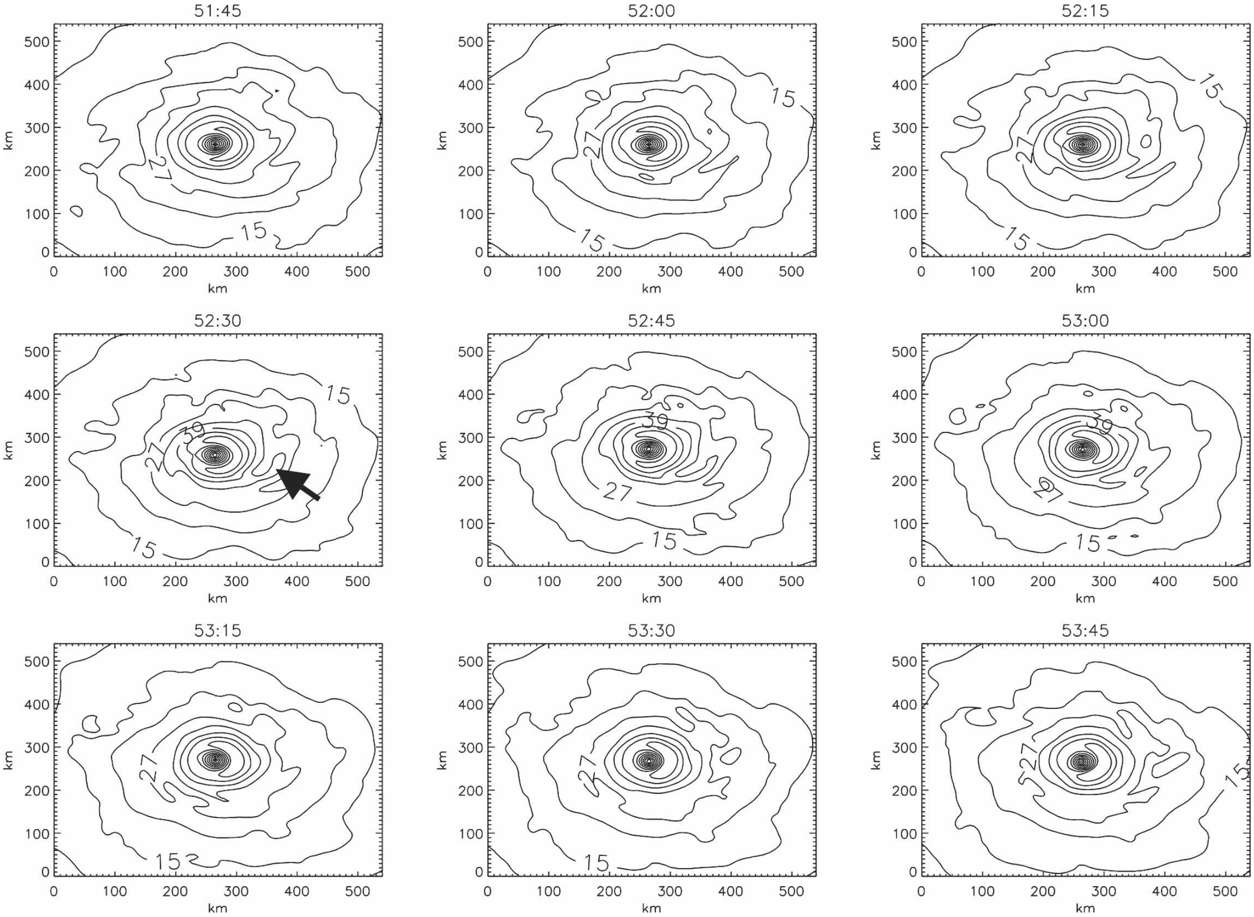

FIG. 6. Tangential velocity at the 600-hPa level (contour interval 6 m s^{-1}). The arrow at time 52 h 30 min refers to the point in between the vorticity couplet at this time and height.

sponsible for the development of the jet and maintains the vorticity couplet once it has been generated. It has been suggested that if the vortices are close enough together, their flow fields can reinforce each other (Weisman and Davis 1998), and this may be an additional source of convergence at the midlevels, which helps to maintain the jet. In addition, while the overall vorticity field associated with the jet is cyclonic, the radial shearing of the tangential winds provides a perturbation to the background vorticity that helps to maintain the cyclonic–anticyclonic vorticity couplet. The jet may play a role in the evolution of the storm by providing a means to transport vorticity to the lower, inner levels of the tropical cyclone as discussed in section 4. Therefore, if the vorticity couplet is working to enhance the lifetime and intensity of the jet, it could be helping to intensify the storm.

4) SENSITIVITY EXPERIMENT

The development of anticyclonic vorticity in squall-line simulations has been attributed to the easterly shear, which was generated by the negative buoyancy of the low-level cooling (e.g., Davis and Weisman 1994; Trier et al. 1997). Cooling below the freezing level is partly caused by evaporation (Leary and Houze 1979) and Yang and Houze (1995) demonstrated that evaporation was the most important latent cooling process in determining the strength of the rear inflow in their simulations. A sensitivity experiment was carried out to test the effect that cloud evaporation has on the generation of mesoscale anticyclones and the midlevel jet. The simulation uses the 46-h fields from the control experiment and then turns off the evaporation of rain and melting graupel and snow. Comparing the spatial extent and intensity of the anticyclonic vorticity (see Fig. 7) with that of the control run, it appears that evaporation is the dominant thermodynamical process responsible for generating the anticyclonic vorticity. This result is consistent with several squall-line modeling studies that have demonstrated the importance of thermal forcing in generating line-end vortices (e.g., Weisman and Davis 1998; Pandya et al. 2000). The lack

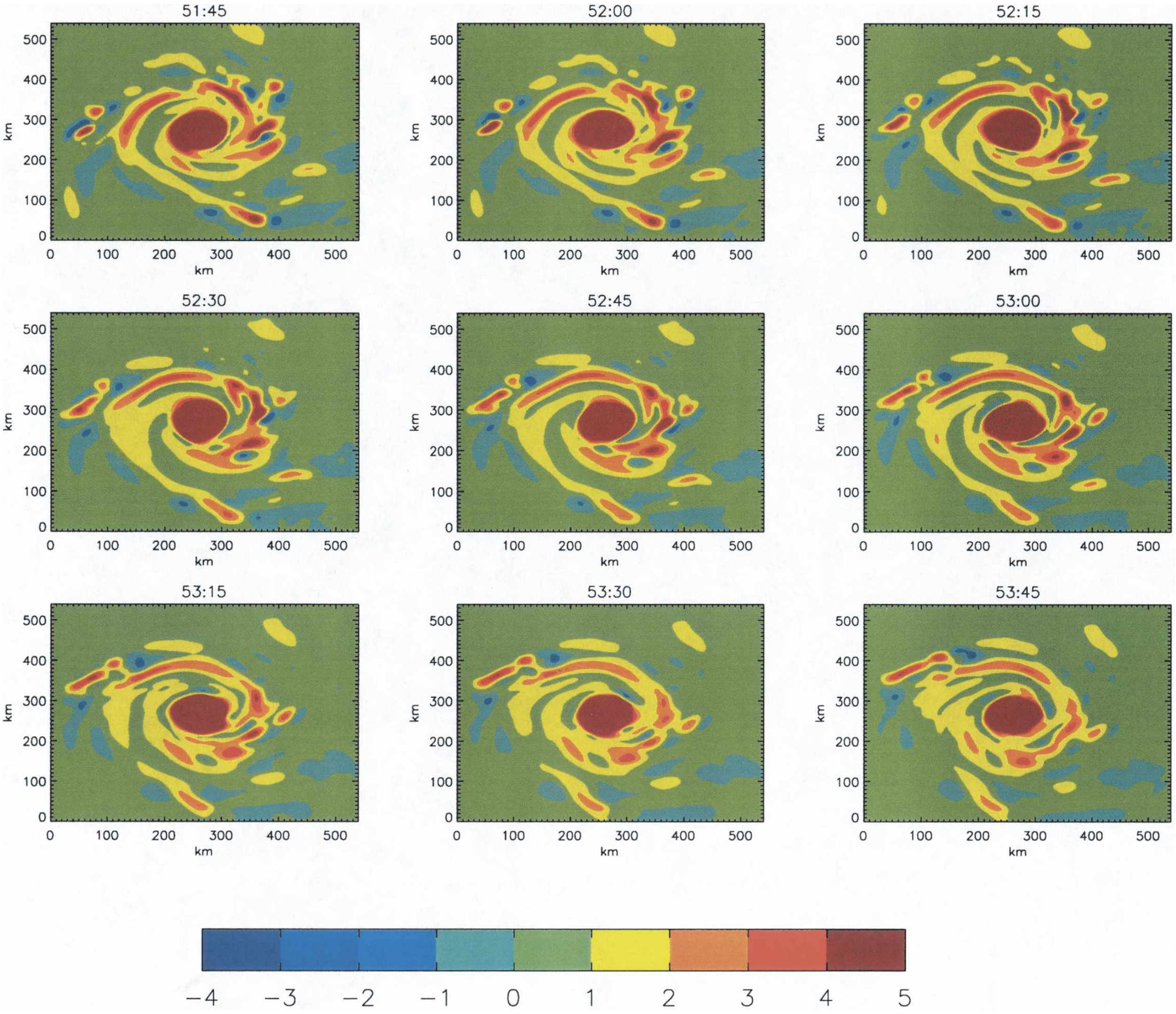

FIG. 7. Vertical component of absolute vorticity ($\times 10^{-4}$ s^{-1}) at the 600-hPa level for the sensitivity experiment with no evaporation. The white regions represent values $<-4 \times 10^{-4}$ s^{-1}, while values $\geq 4 \times 10^{-4}$ s^{-1} are indicated by the darkest color.

of substantial cooling in the low levels reduces the strength of the horizontal vorticity lines, which are needed to generate the vorticity couplet.

Examination of the tangential wind field between 600 and 800 hPa for this experiment (not shown) shows no evidence of a midlevel jet. This demonstrates the importance of evaporation in the diabatic forcing needed to develop the jet as discussed in section 4. The weaker convergence in the midlevels of this simulation is not strong enough to accelerate the flow and there is no development of a jet.

4. Potential vorticity budget

Further illumination of the dynamics of the jet and the rainband can be gained by using PV thinking (Hoskins et al. 1985). The generation of vorticity by the tilting of horizontal vortex lines into the vertical is linked to the generation of PV by horizontal gradients of diabatic heating in the presence of vertical shear (Davis and Weisman 1994). However, the diabatic term of the PV equation also incorporates the generation of PV due to gradients of vertical heating and thus the contributions from diabatic forcing also include the sources (sinks) of vorticity through convergence (divergence). In this section we examine the PV budgets to further elucidate, from the vorticity budgets, which mechanisms are responsible for the generation of PV within the bands and the development of the midlevel jet.

a. PV budgets

The expanded hydrostatic PV equation and its tendency are given by

$$q = -\frac{g}{p_s}\left[-\frac{\partial v}{\partial \sigma}\frac{\partial \theta}{\partial x} + \frac{\partial u}{\partial \sigma}\frac{\partial \theta}{\partial y} + \left(\frac{\partial v}{\partial x} - \frac{\partial u}{\partial y} + f\right)\frac{\partial \theta}{\partial \sigma}\right], \tag{2}$$

$$\begin{aligned}\frac{dq}{dt} &= \frac{\partial q}{\partial t} + u\frac{\partial q}{\partial x} + v\frac{\partial q}{\partial y} + \dot{\sigma}\frac{\partial q}{\partial \sigma}\\ &= -\frac{g}{p_s}\left[-\frac{\partial v}{\partial \sigma}\frac{\partial \dot{\theta}}{\partial x} + \frac{\partial u}{\partial \sigma}\frac{\partial \dot{\theta}}{\partial y} + \left(\frac{\partial v}{\partial x} - \frac{\partial u}{\partial y} + f\right)\frac{\partial \dot{\theta}}{\partial \sigma}\right]\\ &\quad - \frac{g}{p_s}\left[-\frac{\partial F_y}{\partial \sigma}\frac{\partial \theta}{\partial x} + \frac{\partial F_x}{\partial \sigma}\frac{\partial \theta}{\partial y} + \left(\frac{\partial F_y}{\partial x} - \frac{\partial F_x}{\partial y}\right)\frac{\partial \theta}{\partial \sigma}\right],\end{aligned} \tag{3}$$

where q is PV; g is gravity; p_s is surface pressure; t is time; the three wind components are u, v, and $\dot{\sigma}$, and the corresponding spatial variables are x, y, and σ; f is the Coriolis force; θ is potential temperature; $\dot{\theta}$ is the warming expressed as the material change in θ; and F represents the three-dimensional frictional forces. The terms of the budget in Eq. (3) are the local rate of change of PV plus the change in PV due to the advection of PV in the horizontal and vertical balanced by the change in PV due to diabatic heating plus the change in PV due to frictional forces. A conceptual model of the contributions to the diabatic term is shown in Fig. 8. The first process from the left represents convection. Because convection is dominated by condensational heating, which has a maximum in the midtroposphere, the convective region creates a source of PV at the lower levels and a sink at the upper levels (Haynes and McIntyre 1987). The second mechanism is latent heat release in stratiform clouds. With heating due to condensation in stratiform rain occurring mostly above the melting level, this induces a source of PV in the upper troposphere. This diabatic process is complemented by the evaporation and melting of stratiform precipitation, indicated in Fig. 8 by the third process. Evaporation and melting produce a PV source at the base of the cloud. The fourth process that contributes to the diabatic generation of PV is radiation, which moves PV from the stratiform cloud to higher and lower levels (Raymond and Jiang 1990). The top of the cloud cools, creating a PV sink in the stratiform cloud, while the base of the cloud warms producing another sink of PV (Webster and Stephens 1980; Houze 1982). It should be noted that a complete separation of the terms of the PV budget equation is impossible since, for example, a generation of PV from diabatic sources will in turn induce a change in the advective flow and these effects are intimately coupled.

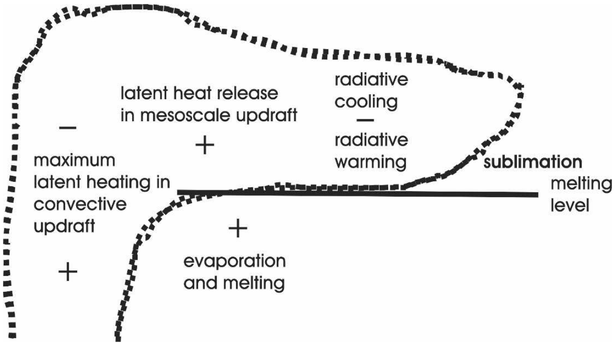

FIG. 8. Schematic of the mechanisms contributing to the generation of PV by diabatic processes. See text for details.

The horizontal and vertical advection terms of the PV budget equation are discretized using the same schemes as in the model (second-order-conservative finite differences). All other derivatives are calculated using second-order centered differences. The budget is calculated using model output at 5-min intervals on σ surfaces. Although this makes the interpretation of the advective terms more difficult, because PV is not conserved between σ surfaces, the advantage is that the data do not need to be interpolated to θ surfaces, reducing further approximations. There has been some discussion in the literature (e.g., Schade 1994; Guinn and Schubert 1994) as to what type of PV is best used in the study of tropical cyclones: dry potential vorticity or saturation equivalent potential vorticity. In this study the dry PV form is chosen because the stratiform regions in the rainbands predominately consist of unsaturated air.

b. *Results and analysis of PV budgets*

To investigate the structure of generated PV anomalies in tropical cyclone rainbands, results are shown for the time 53 h 15 min in the second half of the band's lifetime, where it is mostly of a stratiform nature. As first discussed by Atlas et al. (1963), the stratiform downwind section of the rainband is a result of the detraining ice particles from the convective cells that are advected downwind creating the bright band when they melt below the freezing level. Figure 9 shows the surface reflectivity at the time of interest. The black line represents a slice along a logarithmic spiral with a crossing angle of 22° and the slice is oriented from downwind to upwind. The radii from the center of the storm at the end points of this slice are 61 and 179 km. The vertical motion at this time has a stratiform signature (see Fig. 10a) exhibiting a distinct updraft–downdraft couplet across the melting level.

The potential vorticity structure for the slice shows a region of negative PV centered at about 25 km along the slice (Fig. 10b). This anticyclonic parcel of air

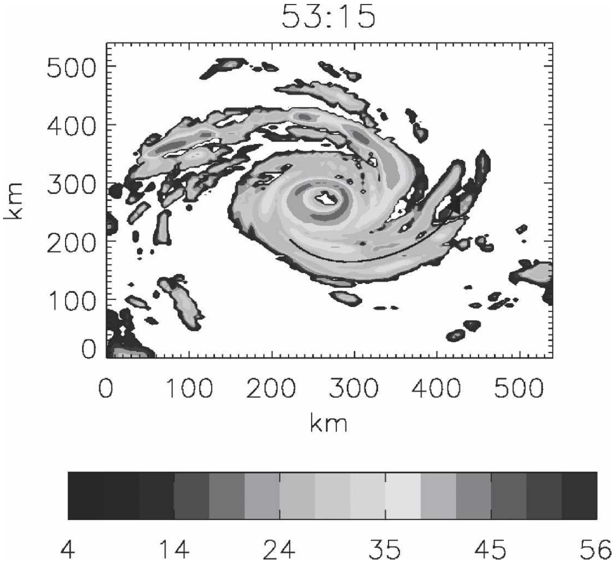

FIG. 9. Pseudo–radar reflectivity (dBZ) at the surface at 53 h 15 min.

moves downwind at a rate calculated from a time series of PV plots as 27.8 m s^{-1}, which is close to the calculated tangential phase speed of 24.2 m s^{-1} for the outer vortex Rossby wave discussed in section 5b. The numerical results of Davis and Weisman (1994) show that although potential temperature changes are constrained to be small because of the near-neutral ascent, heating rates and thus PV generation rates are not and this leads to the production of balanced cyclonic or anticyclonic vortices because most of the generated PV is from vertical vorticity generation rather than stability generation. An important result of their work is the suggestion that the longevity of vortices is not ultimately dependent on the presence or absence of inertial stability. They found that on scales of 50–100 km, anticyclonic vortices with negative PV were as equally balanced as cyclonic vortices and just as likely to persist. The coherence of the negative PV in our band and the similarity between the PV and the relative vorticity fields supports this idea. The persistence of the vorticity couplet is directly linked to the strength and maintenance of the jet, which in turn could have an effect on the vortex as a whole through the transport of vorticity to the inner core of the storm (see section 4). In addition, the longevity of the vorticity couplet has an effect on the generated vortex Rossby waves and the role that they may play in intensifying the storm through wave-mean flow interactions and eyewall replacement cycles as discussed in section 5.

Examination of the horizontal and vertical advection term of the PV tendency equation (Fig. 11b) shows the impact that the anticyclonic mesovortex has on the budget. The region of anticyclonic PV is represented in the advection term at the place where the largest gradient occurs. The downshear-sloping positive and negative advective regions associated with the instability extend from 400 to about 800 hPa. These large advective terms are balanced predominately by the local time derivative of q (see Fig. 11a). However, the magnitude of the $\partial q/\partial t$ term is significantly smaller than that of the advection term in the region of the anticyclonic PV and this results in the remainder of the budget equation (Fig. 11e) displaying a pattern that is the same as the advective term.

Figure 11c shows the diabatic term of the PV tendency equation. The region between 50 and 120 km is consistent with the theory of Raymond and Jiang (1990) that expects cyclonic PV generation near the melting level within the stratiform rain area and anticyclonic PV generation below. However, there is also significant structure superimposed on this theoretical composition due to the complexity of the background PV cross section (see Fig. 10b). At 53 h 15 min the generation of PV from diabatic sources within the troposphere in the band is of the same magnitude as the diabatic sinks of PV; however, the sources cover a larger area. Thus, at this period of the band's lifetime, when it displays a uniform stratiform precipitation structure, it seems that the diabatic processes within the band are playing a positive role in the maintenance and intensification of the storm by creating a source of cyclonic PV in the midlevels where it could then be advected into the inner, lower levels of the cyclone. Fig. 11c illustrates the hypothesis of May and Holland (1999) that the diabatic production of PV is responsible for the generation of the midlevel jet. There is a band of cyclonic PV production that begins below 500 hPa at the outer end of the band and extends right through the band, sloping down toward the low levels at the end near the inner core of the cyclone. The generation rate of cyclonic PV in the low levels of the downwind end of the band by diabatic forcing equates to more than 3 potential vorticity units (PVU) per hour, which is larger than the maximum observed value of 0.4 PVU h^{-1} calculated by May and Holland (1999). This difference is due to the omission of the horizontal heating gradients in their study, which contributes to the production of cyclonic PV in the midlevels.

The vertical component of diabatic heating generates the major contribution at the melting layer (not shown). The horizontal component reflects the generation of vorticity through the tilting of horizontal vortex lines into the vertical and the fact that this term is producing the majority of the anticyclonic vorticity is consistent with previous results showing that the horizontal

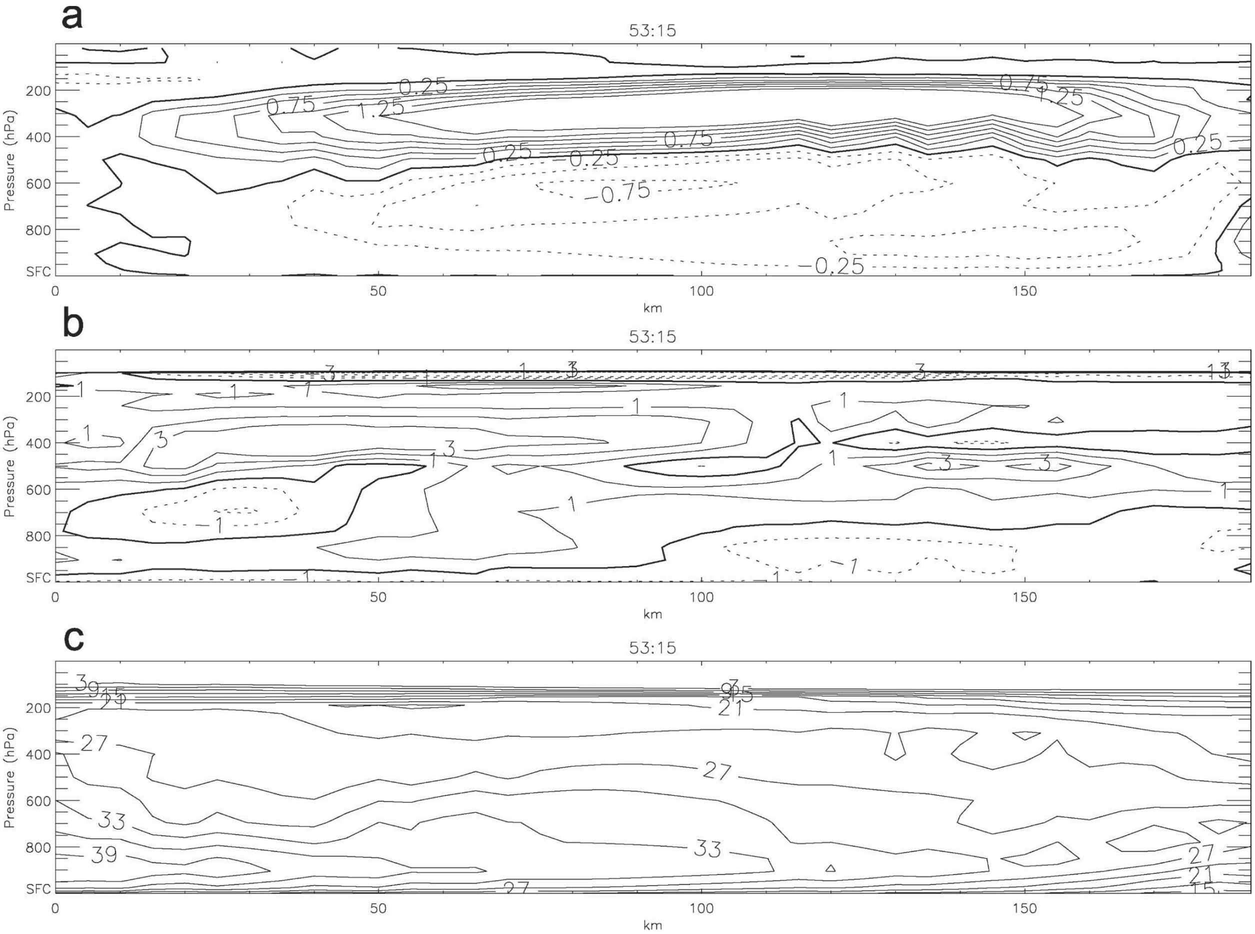

FIG. 10. (a) Vertical velocity along the slice in Fig. 11 (contour interval 0.25 m s^{-1}), (b) potential vorticity (contour interval 1 PVU), and (c) tangential velocity (contour interval 3 m s^{-1}).

vortex lines caused by the buoyancy gradients between the evaporatively cooled downdraft and the mesoscale updraft are responsible for the creation of anticyclonic vorticity (Weisman 1992). The results presented here also agree with the conceptual model in Fig. 8, with cyclonic PV being dumped at the base of the anvil cloud.

The development of the midlevel jet in the band at 53 h 15 min from 50 to 120 km arises from the production of PV by the diabatic term (see Fig. 11c). This only occurs once the rainband is predominately of a stratiform structure. Analysis of the tangential velocity field illustrates that the jet in our rainband is a rear-inflow jet in the sense that it flows through the stratiform region, descending as it approaches the convective motions farther downwind in the band (Fig. 10b). Rear-to-front jets are often associated with mesoscale convective complexes, which rainbands emulate (e.g., Powell 1990a). Such rear-to-front jets are usually associated with evaporation and melting in the downdraft and the resulting diabatic production of PV (Raymond 1992). As discussed earlier, the generation of anticyclonic vorticity at the low levels was a consequence of the horizontal gradient of heating in the presence of vertical shear and resulted primarily from evaporation. The development and strength of the jet are enhanced by the production of cyclonic PV in the midlevels. Therefore, both heating and cooling play an important role in driving the jet.

Friction is the smallest term in the PV budget in the rainband region (Fig. 11d). Processes contributing to frictional PV generation include mixing across regions of strong horizontal and vertical shear and surface friction. The most important part of the frictional PV generation is the enhancement of the cyclonic PV production along the 500-hPa level at the outer end of the band and sloping to the lower levels in the inner region, as seen in the diabatic term and the advective term. It is interesting to note that all of the components of the PV budget exhibit a line where $dq/dt = 0$, generally

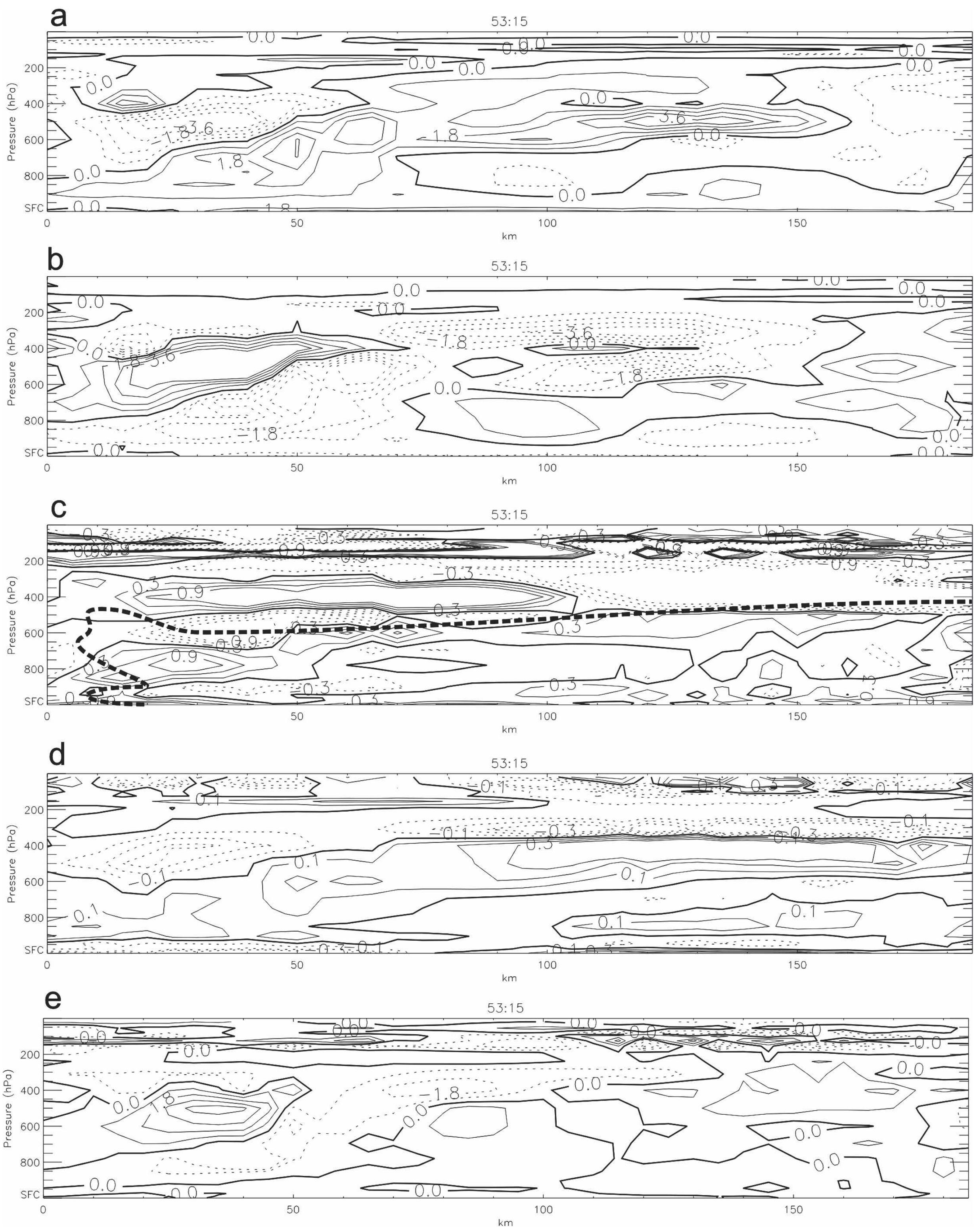

FIG. 11. (a) Local time derivative of the PV tendency equation for the slice in Fig. 11 ($\times 10^{-3}$ PVU s^{-1}; contour interval 0.9; negative values are represented by dashed lines and the zero line is boldface), (b) horizontal and vertical advection terms of the PV tendency equation ($\times 10^{-3}$ PVU s^{-1}; contour interval 0.9), (c) diabatic term ($\times 10^{-3}$ PVU s^{-1}; contour interval 0.3) with the 0 cm s^{-1} vertical velocity contour (dashed line), (d) friction term ($\times 10^{-3}$ PVU s^{-1}; contour interval 0.1), and (e) the remainder of the PV tendency equation ($\times 10^{-3}$ PVU s^{-1}; contour interval 0.9).

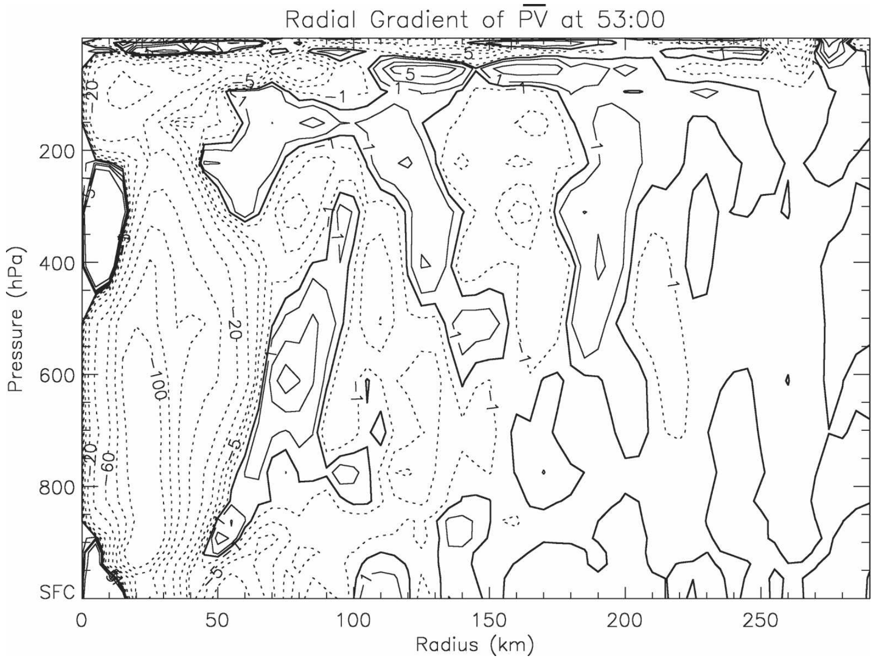

FIG. 12. Radial gradient of symmetric potential vorticity at the 600-hPa level ($\times 10^{-5}$ PVU m^{-1}) at 53 h 00 min. Contour intervals are -100, -80, -60, -40, -20, -10, -5, -3, -1, 0, 1, 3, and 5.

sloping from the outer midlevels of the band down to the inner low levels. This feature is relatively consistent over time and represents a steady state, separating the PV generation mechanisms above and below this level.

5. Vortex Rossby wave characteristics

The previous sections discussed rainband structure and PV generation; this section relates to processes controlling the formation and organization of the rainbands. In tropical cyclones, maximum values of PV are found near the center of the vortex with a generally monotonic decrease with radius outside of the radius of maximum winds. If this basic state is perturbed, there is a restoring effect and PV or vortex Rossby waves propagate (MacDonald 1968; Guinn and Schubert 1993). The only full-physics model verification of vortex Rossby waves are the recent studies of Chen and Yau (2001) and Wang (2001, 2002). Chen and Yau (2001) showed the presence of inward- and outward-propagating vortex Rossby waves associated with inner tropical cyclone rainbands that were excited by convectively generated PV asymmetries in the eyewall region. Wang (2001) identified vortex Rossby waves in the inner core of a tropical cyclone. He also found that the wave energy propagates inward in contrast to the theoretical results of Montgomery and Kallenbach (1997). These waves can flux eddy vorticity toward the eyewall (Schubert et al. 1999); hence, the rainbands may play a role in the intensification of the tropical cyclone.

Figure 12 shows the radial derivative of the mean state, $\bar{q}'(R)$, at 53 h 00 min. The decrease of PV with radius is most pronounced in the lower troposphere at the 25-km radius. The value of $\bar{q}'(R)$ is strongly negative in the eyewall where the high PV of the vortex core decreases quickly. The gradient is positive in a region between the eyewall and the rainband where the vorticity is increasing to the secondary maximum in the band. This implies that prograde waves may not only be generated inside the eye where $\bar{q}'(R)$ is positive (Chen and Yau 2001), but also on the inner side of rainbands.

Montgomery and Kallenbach (1997) derived a local dispersion relation for vortex Rossby waves in a two-dimensional barotropic model using Wenzel–Kramers–Brillouin analysis and in an asymmetric balanced shallow-water model. Möller and Montgomery (2000) have extended these results to a three-dimensional stably stratified barotropic vortex in gradient and hydrostatic balance. Their derived local dispersion relation is

$$\omega = n\bar{\Omega} + \frac{n}{r}\frac{\bar{\xi}}{\bar{q}}\frac{\bar{q}'(R)}{[k^2 + n^2/R^2 + (\bar{\eta}\bar{\xi}m^2)/N^2]}, \qquad (4)$$

where ω is the local wave frequency, an overbar denotes mean state quantities, n is the azimuthal wavenumber, m the vertical wavenumber, k the time-dependent radial wavenumber [$k = k_0 - nt\bar{\Omega}'(R)$], $\bar{\Omega}$ is mean angular velocity, $\overline{\Omega}'(R)$ is the radial gradient of the mean angular velocity, R the reference radius, $\overline{\eta}$ is the mean absolute vorticity ($\overline{\eta} = \overline{\zeta} + f$, where f is the Coriolis force and $\overline{\zeta}$ is the mean vertical component of relative vorticity), $\overline{\xi}$ is the mean inertial parameter ($\overline{\xi} = f + 2\overline{\upsilon}_t/R$), N^2 is the static stability, and $\overline{q}$ and $\overline{q}'(R)$ represent the mean potential vorticity and its radial gradient at radius R. The radial wavenumber k changes with time due to the shearing and stretching of the waves by the vortex, which tend toward symmetrization (Montgomery and Kallenbach 1997).

a. Verification of vortex Rossby waves

A time series of the magnitude of the absolute vorticity of the asymmetric component of the wind at 600 hPa is shown in Fig. 13. At 51 h 00 min into the simulation the rainband is located between the outer edge of the eyewall at the 50- and 150-km radii. Apart from the largest contribution associated with the inner core of the storm, there are two pulses of asymmetric vorticity coincident with the rainband location (Fig. 13). The largest perturbation associated with the band at this time occurs between the radii of 90 and 135 km. This area incorporates the majority of the band and the peak in Fig. 13 at 51 h 45 min is aligned with the region of anticyclonic absolute vorticity discussed in section 3. This region of anticyclonic vorticity, and associated potential vorticity, will perturb the basic state of the PV and generate a propagating wave. Analysis of the perturbation absolute vorticity for earlier times, when there is no significant anticyclonic vorticity, shows no evidence of a secondary peak associated with the rainband. Over time the inner anomaly moves outward and the outer anomaly moves inward. While the magnitude of the outer peak remains fairly constant over time, the inner anomaly increases from significantly less than the outer peak initially, to a greater magnitude at 52 h 30 min–52 h 45 min. From 53 h 15 min onward (not shown), the band decays and the anomalies merge together leaving only one peak associated with the band.

Analysis of the Fourier decomposition of the absolute vorticity field reveals that the inner peak in the asymmetric or perturbation component shown in Fig. 13 is made up of contributions primarily from azimuthal wavenumbers 1 and 3, and to a lesser extent wavenumber 2 (see Fig. 14). Wavenumber one will be partly made up of the beta gyre (Fiorino and Elsberry 1989). The outer peak has large contributions from azimuthal wavenumbers 4, 6, and 8 as well as some contributions from the smaller wavenumbers. The following subsections diagnose the properties of these waves associated with the rainband and discuss the implications of their kinematics on the evolution of the tropical cyclone.

b. Outer wave properties

The outer, upwind region of anticyclonic vorticity discussed earlier coincides with the outer vorticity anomaly in Fig. 13. To investigate the wave kinematics associated with this outer rainband anomaly we take the azimuthal mean quantities at 51 h 45 min at $R = 120$ km and the 600-hPa level: $\overline{\upsilon}_t = 25$ m s^{-1}, $N^2 = 2 \times 10^{-5}$ s^{-1}, $\overline{\xi} = 4 \times 10^{-4}$ s^{-1}, $\overline{\eta} = 1.0 \times 10^{-4}$ s^{-1}, $\overline{q} = 1$ PVU, and $\overline{q}' = -4 \times 10^{-5}$ PVU m^{-1}. The radial and vertical wavenumbers have been determined from the plots of the magnitude of the individual Fourier components. Analysis of these plots over the lifetime of the wave gives a negative sign of both k and m. The wavelengths are estimated to be $\lambda_{\text{radial}} = 50$ km and $\lambda_{\text{vertical}} = 6$ km for the time of interest. Using (4) for $n = 4$ gives an apparent vortex Rossby wave frequency of $\omega = 8.19 \times 10^{-4}$ s^{-1}. The period is then $2\pi/\omega = 2.2$ h. The lifetime of the band is less than 4 h, so the linear approximation used to describe the wave is too short to describe the rainband; however, the anticyclonic vorticity exists for around 2.75 h. The apparent azimuthal phase speed of 24.6 m s^{-1} is consistent with the phase speed of 26.5 m s^{-1} gained from the time series of the η_a plots. The radial phase speed calculated from $C_{pr} = \omega/k$ is -6.4 m s^{-1}. Using the $n = 4$ plots of the asymmetric absolute vorticity $C_{pr} = -5.5$ m s^{-1} (negative indicates inward propagation of the leading spiral). The vertical propagation of the wave, $C_{pz} = \omega/m$, is -0.8 m s^{-1}. Visual inspection of cross sections taken along the rainband shows that the wave is a downstream-tilted PV anomaly and moves slowly downward. The top boundary of the model is $\sigma = 0$ and the only condition required is that $\dot{\sigma} = 0$. This condition does allow waves to be reflected, but there is sufficient resolution in the stratosphere (four levels) to absorb these waves before reaching the top of the atmosphere. This is verified by the fact that there is no evidence of these waves propagating above 100 hPa. While the dynamics of the rainband are nonlinear, the agreement that we see between the modeled wave and the theory indicates that the linear wave theory captures a significant part of the dynamics associated with the asymmetric PV disturbances.

The dispersion relation (4) can also be used to find the three-dimensional group velocities. Recalling that $k = k_0 - nt\overline{\Omega}'(R)$, the azimuthal group velocity is

$$
\begin{aligned}
C_{g\lambda} &= \frac{\partial \omega}{\partial (n/R)} \\
&= \overline{\upsilon}_t + \frac{\overline{\xi}}{\overline{q}} \frac{\overline{q}'(R)}{[k^2 + n^2/R^2 + (\overline{\eta}\,\overline{\xi} m^2)/N^2]^2} \\
&\quad \times \left[k_0^2 + (\overline{\eta}\,\overline{\xi} m^2)/N^2 - \frac{n^2}{R^2}(1 + t^2 R^2 \overline{\Omega}^2) \right]. \qquad (5)
\end{aligned}
$$

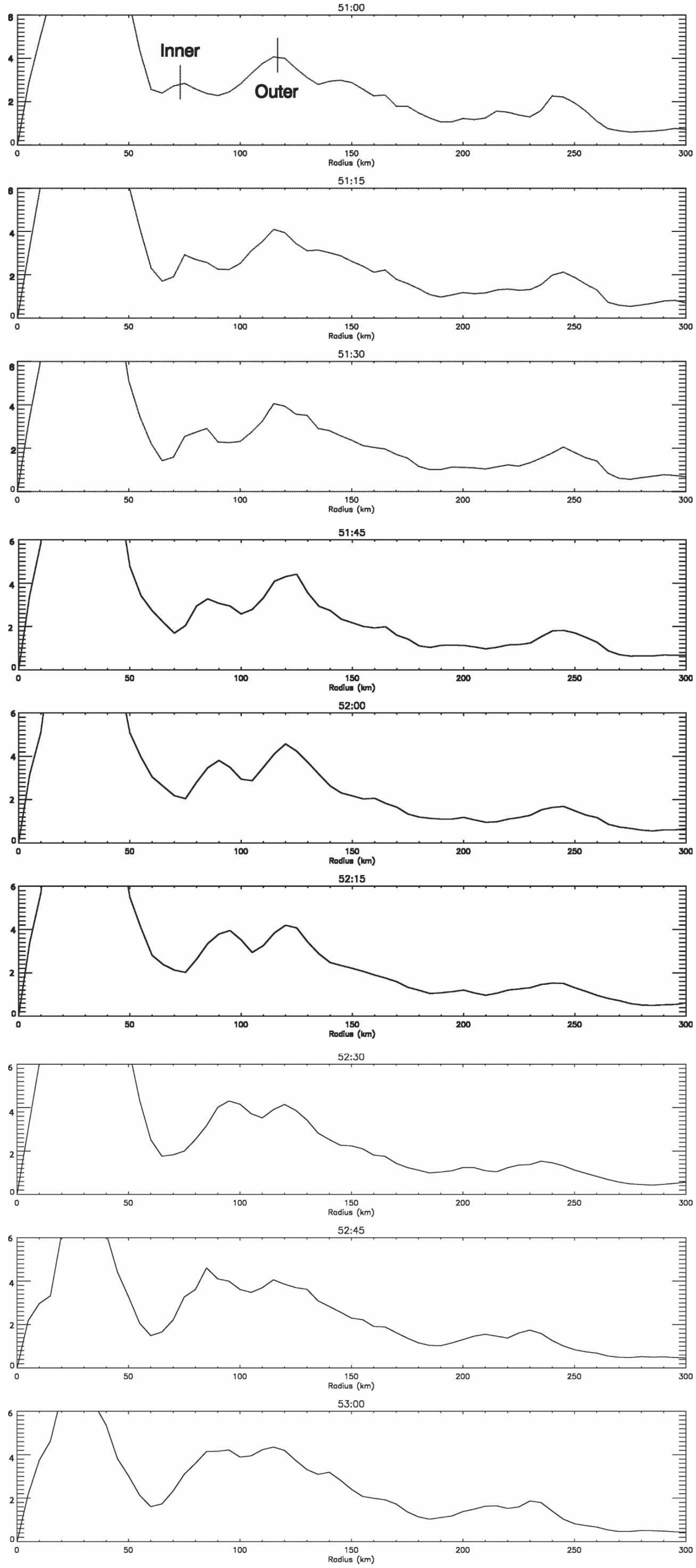

FIG. 13. Magnitude of the asymmetric absolute vorticity at the 600-hPa level ($\times 10^{-4}$ s^{-1}) for the times 51 h 00 min to 53 h 00 min. The inner and outer perturbations associated with the rainband are labeled in the first panel.

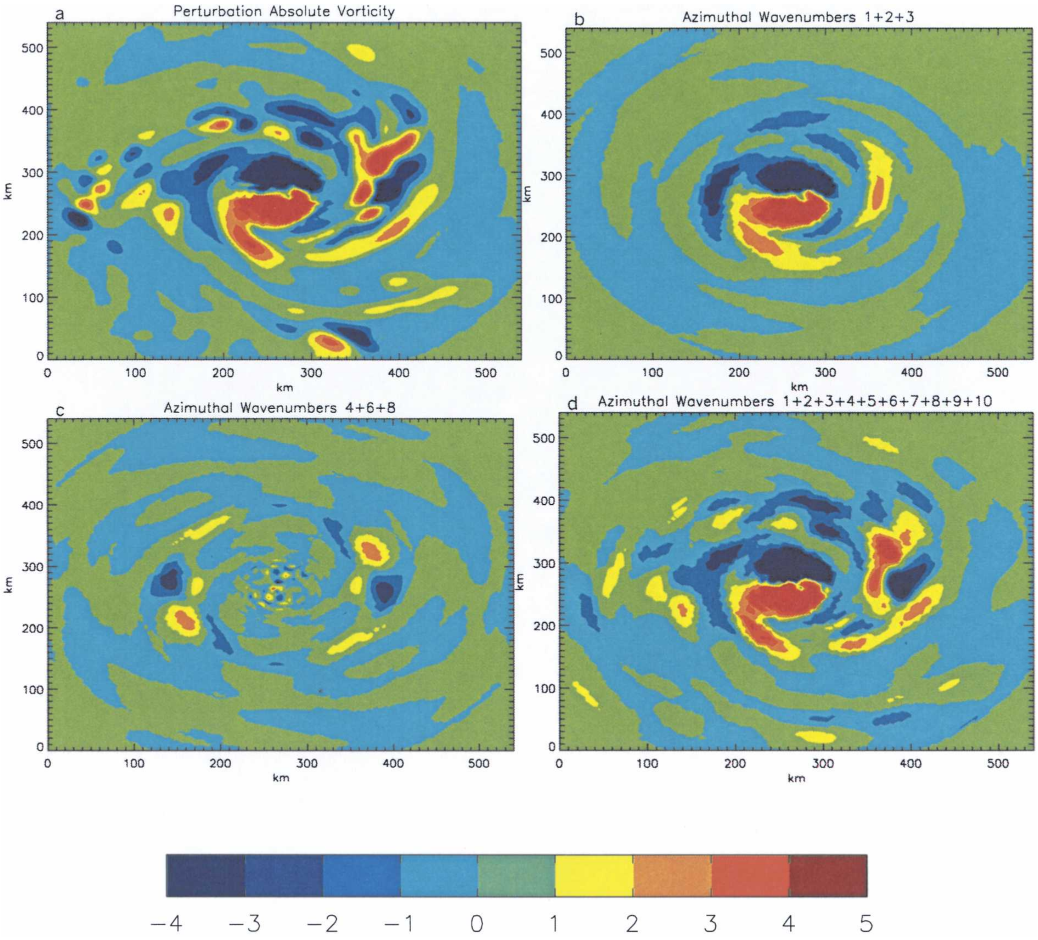

FIG. 14. (a) Perturbation absolute vorticity, (b) azimuthal wavenumbers 1 + 2 + 3, (c) wavenumbers 4 + 6 + 8, and (d) wavenumbers 1–10 at the 600-hPa level ($\times 10^{-4}$ s^{-1}), at 52 h 15 min.

If we treat (5) as an initial value problem, $C_{g\lambda}$ has a value of 24.3 m s^{-1}, which is less than $\bar{\upsilon}_t$ because $k = k_0$ is the dominant wavenumber. Initially as t increases, the azimuthal group velocity will be greater than $\bar{\upsilon}_t$, although in the limit $t \rightarrow \infty$, the group velocity will continue to increase as long as $k \rightarrow 0$ while the wave propagates inward. Möller and Montgomery (1999) found that the initially inward-traveling waves changed the sign of their radial wavenumbers and then began an outward propagation; however, it appears that our wave decays while it is still a leading spiral. The theoretically derived vertical group velocity is -3.1×10^{-3} m s^{-1}, and thus the wave is moving energy very slowly to the lower levels.

Theoretically calculating the radial group velocity gives $C_{gr} = 0.2$ m s^{-1}, so that both the radial and azimuthal group velocities are much slower than the phase speeds of $n = 4$; thus, the wave is dispersive. This indicates that the wave is composed of a number of Fourier components and the energy of the disturbed flow propagates at the group velocity. Over the last hour (53 h 00 min–54 h 00 min), energy is transferred from the lower to the higher wavenumbers. Because of the dependence of the radial wavenumber on n, the waves become more radially confined as the wavenumber increases. Since this wave is located at approximately 120 km, we expect that the energy associated with this wave will be less likely to penetrate into the inner core of the vortex. However, the energy may intensify the winds outside the radius of maximum wind that could lead to a weakening of the eyewall, as demonstrated by Möller and Montgomery (2000).

c. *Inner wave properties*

To find the properties of the wave located at around 80 km we take the mean-state quantities at 51 h 45 min at $R = 85$ km and the 600-hPa level: $\bar{\upsilon}_t = 32$ m s^{-1}, $N^2 = 2 \times 10^{-5}$ s^{-1}, $\bar{\xi} = 7 \times 10^{-4}$ s^{-1}, $\bar{\eta} = 1.5 \times 10^{-4}$ s^{-1}, $\bar{q} = 1$ PVU, $\bar{q}' = 2 \times 10^{-5}$ PVU m^{-1}, $\lambda_{\text{radial}} = 50$ km, and $\lambda_{\text{vertical}} = 6$ km. Applying the equations for $n = 1$

gives an apparent vortex Rossby wave frequency of $\omega = 3.8 \times 10^{-4}\ \mathrm{s}^{-1}$. The period is then 4.6 h, which fits more closely than the outer wave with the observed rainband period of just less than 4 h. This might suggest that the band is an outward-propagating vortex Rossby wave. At this radius and height the radial gradient of PV is positive. It is the region on the inner side of the band where the PV is increasing from the small values in the moat between the eyewall and the band, to the larger values in the rainband. Therefore, this wave is a prograde wave and the azimuthal phase speed of 32.3 $\mathrm{m\ s^{-1}}$ is faster than the mean tangential wind. Using the plots of the $n = 1$ Fourier component, the radial propagation is 4.4 $\mathrm{m\ s^{-1}}$, which compares well to the value derived from the dispersion relation of 3.0 $\mathrm{m\ s^{-1}}$. The theoretically derived vertical motion of the $n = 1$ wave is downward at $-0.4\ \mathrm{m\ s^{-1}}$, since this wave is also a downstream tilted anomaly.

The theoretically calculated azimuthal group velocity of 0.42 $\mathrm{m\ s^{-1}}$ again shows the dispersive nature of these waves. The radial group velocity is $-0.06\ \mathrm{m\ s^{-1}}$, which is not only much slower than the phase speed, but it is also in the opposite direction, inward. For a positive radial gradient of PV and a positive radial wavenumber k, the radial group velocity is negative. Thus, the energy of this wave propagates into the center of the vortex (Chen and Yau 2001). The theoretically derived vertical group velocity is in the same direction as the vertical phase speed (downward), although the rate of propagation is less, $C_{gz} = -2.6 \times 10^{-3}\ \mathrm{m\ s^{-1}}$. However, this is an order of magnitude faster than the vertical group velocity for the outer wave and shows how this wave can transport energy from outer radii into the inner, lower regions of the storm, providing a mechanism for the band to intensify the storm.

d. Sensitivity case

It is interesting to compare the vortex Rossby wave dynamics with those in the sensitivity case where the evaporation in the clouds was turned off and consequently the anticyclonic absolute vorticity was significantly reduced. The two most significant changes are the magnitude of the asymmetric vorticity and the presence of only one peak in the rainband region (not shown). In the case with evaporation, the perturbation $|\overline{\eta}_a|$ at 53 h 00 min was a maximum of $2.3 \times 10^{-4}\ \mathrm{m\ s^{-1}}$ in the band region, whereas with no evaporation $|\overline{\eta}_a| = 1.3 \times 10^{-4}\ \mathrm{m\ s^{-1}}$. The rainband in the case with evaporation is associated with two vortex Rossby waves, whereas in the case with no evaporation the band is associated with only one wave. It appears to be quasi-stationary and is located at a radius between the two waves of the control case. Because there is significantly less generation of anticyclonic vorticity in the rainband in the sensitivity case, we do not see the same vortex Rossby wave pattern as was shown in section 5b. This reinforces the idea that vorticity anomalies produced by internal rainband dynamics perturb the mean-state PV and induce vortex Rossby waves that can influence the evolution of the storm.

6. Discussion and conclusions

It has been demonstrated in this study that internal band processes in the model can support the development of anticyclonic vorticity that is strong enough to result in inertial instability on the outer sides of rainbands. The primary source of this vorticity is the tilting into the vertical of system-generated horizontal vorticity, which results in a cyclonic–anticyclonic vorticity couplet radially across the band. Once the mesoscale anticyclone has been developed, it is maintained by stretching as it is advected cyclonically downwind. The anticyclonic mesovortex is strained horizontally into a filament as it approaches the center of the storm and is eventually wrapped into the core. The persistence of the mesoscale anticyclone suggests that it is balanced even though it is unstable by normal standards. This supports the findings of Davis and Weisman (1994), who demonstrated that the longevity of anticyclonic mesovortices is not ultimately dependent on the measure of inertial instability and that they may be as equally balanced as cyclonic mesovortices.

The midlevel jet does not appear in the rainbands until the band has matured to a more stratiform structure. The broad region of heating above the 0°C isotherm works in conjunction with the cooling below to accelerate the rear-to-front flow at the midlevels (Lafore and Moncrieff 1989). The height of the jet decreases as it moves downwind and is located radially in between the cyclonic–anticyclonic couplet. It is difficult to determine the effect that the jet has on initiating new convective elements in the band, the longevity of the band, and the cyclone as a whole. However, as Weisman (1992) found in squall-line simulations, the primary role of the jet was to transport horizontal vorticity. In squall lines the jet runs between cyclonic–anticyclonic vortices, feeding vorticity from the rear to the leading edge of the system. In our case when we use the same orientation with respect to the vortices, the jet could transport vorticity azimuthally from the upwind end of the rainband to the downwind end or inner core of the storm, since the rainband takes the form of a logarithmic spiral.

Evaporation in the stratiform precipitation regions was critical to the development of the anticyclonic vorticity features and the midlevel jet. In a sensitivity experiment where cloud evaporation was turned off, the resulting absolute vorticity fields showed a significant reduction in the anticyclonic vorticity component of the rainbands and a coherent couplet of cyclonic–anticyclonic mesovortices did not develop. The tangential velocity at the midlevels for the case with no evaporation also had no evidence of a jet. Thus, we conclude that evaporation is an essential ingredient in developing the cyclonic–anticyclonic vorticity couplet and driving the midlevel jet.

Calculation of the PV budget confirms the hypothesis that the development of the midlevel jet can be described using PV dynamics. The stratiform regions of the bands create a PV dipole, with cyclonic PV at the midlevels and anticyclonic PV below. The lower levels of the downwind end of the rainband generate cyclonic PV, which could help to feed the convection in the inner core of the storm, spinning up strong surface winds and intensifying the vortex. The height of the jet is the same as the diabatically produced cyclonic PV, decreasing to the low levels as the flow nears the center of the cyclone. Because θ surfaces also lower with decreasing radius (e.g., May and Holland 1999), this then allows the accelerated flow to advect the midlevel-generated cyclonic PV from the band to the inner and lower regions of the storm.

Fourier decomposition of the absolute vorticity field showed two counterpropagating waves associated with the outer rainband, propagating on the vorticity gradients generated within the band. These waves were shown to satisfy the vortex Rossby wave theory. The wave located on the inner side of the band was composed of low azimuthal wavenumbers and propagated outward, although the radial group velocity and hence the energy transfer were inward. The outer wave was collocated with the anticyclonic mesovortex and made up predominately of wavenumbers 4, 6, and 8.

The outer wave did not travel inside the 100-km radius and thus did not directly interact with the eyewall. However, idealized modeling studies have demonstrated that outer waves can contribute to the evolution of the tropical cyclone. For example, Smith and Montgomery (1995) showed that higher azimuthal wavenumber disturbances were confined to larger radii because of the damping of the perturbation by strong shear in the process of axisymmetrization. Therefore, the asymmetric vorticity generated in the rainband positively influences the intensification of the storm by contributing to the symmetric component of vorticity. Another way in which the rainband-generated vorticity could affect the intensification cycle of the tropical cyclone is through the development of secondary eyewalls and eyewall replacement (Willoughby et al. 1982). Möller and Montgomery (2000) showed that PV asymmetries outside of the radius of maximum winds acted to intensify the outer tangential winds through wave-mean flow and wave–wave interactions. Their results demonstrated that the change in the primary circulations induced a secondary circulation that resulted in subsidence near the radius of maximum winds, which could weaken the eyewall.

This is the first full-physics modeling study that we know of to show that outer tropical cyclone rainbands are consistent with the vortex Rossby wave theory. Most of the published results investigating this theory in tropical cyclone vortices have used idealized models (e.g., Montgomery and Enagonio 1998; Möller and Montgomery 1999, 2000). Other full-physics modeling studies have focused on inner rainbands and eyewall dynamics (Chen and Yau 2001; Wang 2001, 2002); however, here we have shown that vorticity asymmetries produced by outer rainband dynamics can excite inward- and outward-propagating vortex Rossby waves. Montgomery and Kallenbach (1997) discussed the theory behind environmental asymmetries exciting inward-propagating vortex Rossby waves, but they have not been verified by full-physics models of the atmosphere. Here, we have shown that an internally produced perturbation in the form of an area of anticyclonic vorticity is exciting inward-propagating waves. It is a logical extension that this type of disturbance could be produced by environmental interactions such as upper-level troughs, fronts, and topography.

Acknowledgments. This work was supported by an Australian Postgraduate Research Award. The authors thank Dr. Yuqing Wang for his helpful discussions concerning the numerical model TCM3 and also thank two anonymous reviewers whose comments greatly improved the manuscript.

REFERENCES

Atlas, D., K. R. Hardy, R. Wexler, and R. J. Boucher, 1963: On the origin of hurricane spiral bands. *Geofis. Int.,* **3,** 123–132.

Barnes, G. M., J. F. Gamache, M. A. LeMone, and G. S. Stossmeister, 1991: A convective cell in a hurricane rainband. *Mon. Wea. Rev.,* **119,** 776–794.

Braun, S. A., and R. A. Houze Jr., 1997: The evolution of the 10–11 June 1985 PRE-STORM squall line: Initiation, development of rear inflow, and dissipation. *Mon. Wea. Rev.,* **125,** 478–504.

Chen, Y., and M. K. Yau, 2001: Spiral bands in a simulated hurricane. Part I: Vortex Rossby wave verification. *J. Atmos. Sci.,* **58,** 2128–2145.

Davis, C. A., and M. L. Weisman, 1994: Balanced dynamics of mesoscale vortices produced in simulated convective systems. *J. Atmos. Sci.,* **51,** 2005–2030.

Emanuel, K. A., 1983: The Lagrangian parcel dynamics of moist symmetric instability. *J. Atmos. Sci.,* **40,** 2368–2376.

Fiorino, M., and R. L. Elsberry, 1989: Some aspects of vortex structure related to tropical cyclone motion. *J. Atmos. Sci.,* **46,** 975–990.

Frank, W. M., 1977: The structure and energetics of the tropical cyclone. I: Storm structure. *Mon. Wea. Rev.,* **105,** 1119–1135.

Franklin, C. N., G. J. Holland, and P. T. May, 2005: Sensitivity of tropical cyclone rainbands to ice-phase microphysics. *Mon. Wea. Rev.,* **133,** 2473–2493.

Gamache, J. F., and R. A. Houze Jr., 1982: Mesoscale air motions associated with a tropical squall line. *Mon. Wea. Rev.,* **110,** 118–135.

Guinn, T. A., and W. H. Schubert, 1993: Hurricane spiral bands. *J. Atmos. Sci.,* **50,** 3380–3403.

——, and ——, 1994: Reply. *J. Atmos. Sci.,* **51,** 3545–3546.

Haynes, P. H., and M. E. McIntyre, 1987: On the evolution of vorticity and potential vorticity in the presence of diabatic heating and friction or other forces. *J. Atmos. Sci.,* **44,** 828–841.

Holland, G. J., 1997: Maximum potential intensity of tropical cyclones. *J. Atmos. Sci.,* **54,** 2519–2541.

Holton, J. R., 1992: *An Introduction to Dynamic Meteorology*. 3d ed. Academic Press, 511 pp.

Hoskins, B. J., 1974: Role of potential vorticity in symmetric stability and instability. *Quart. J. Roy. Meteor. Soc.,* **100,** 480–482.

——, M. E. McIntyre, and A. W. Robertson, 1985: On the use and significance of isentropic potential vorticity maps. *Quart. J. Roy. Meteor. Soc.,* **111,** 877–946.

Houze, R. A., Jr., 1982: Cloud clusters and large-scale vertical motions in the tropics. *J. Meteor. Soc. Japan,* **60,** 396–410.

Jorgensen, D. P., 1984: Mesoscale and convective-scale characteristics of mature hurricanes. Part I: General observations by research aircraft. *J. Atmos. Sci.,* **41,** 1268–1285.

——, M. A. LeMone, and S. B. Trier, 1997: Structure and evolution of the 22 February 1993 TOGA CORE squall line: Observations of precipitation, circulation, and surface energy. *J. Atmos. Sci.,* **54,** 1961–1985.

Kingsmill, D. E., and R. A. Houze Jr., 1999: Kinematic characteristics of air flowing into and out of precipitating convection over the west Pacific warm pool: An airborne Doppler radar study. *Quart. J. Roy. Meteor. Soc.,* **125,** 1165–1207.

Lafore, J.-P., and M. W. Moncrieff, 1989: A numerical investigation of the organization and interaction of the convective and stratiform regions of tropical squall lines. *J. Atmos. Sci.,* **46,** 521–544.

Leary, C. A., and R. A. Houze Jr., 1979: The structure and evolution of convection in a tropical cloud cluster. *J. Atmos. Sci.,* **36,** 437–457.

MacDonald, N. J., 1968: The evidence for the existence of Rossby-like waves in the hurricane vortex. *Tellus,* **20,** 138–146.

Marks, F. D., Jr., 1985: Evolution of the structure of precipitation in Hurricane Allen (1980). *Mon. Wea. Rev.,* **113,** 909–930.

May, P. T., 1996: The organization of convection in the rainbands of Tropical Cyclone Laurence. *Mon. Wea. Rev.,* **124,** 807–815.

——, and D. K. Rajopadhyaya, 1996: Wind profiler observations of vertical motion and precipitation microphysics of a tropical squall line. *Mon. Wea. Rev.,* **124,** 621–633.

——, and G. J. Holland, 1999: The role of potential vorticity generation in tropical cyclone rainbands. *J. Atmos. Sci.,* **56,** 1224–1228.

——, ——, and W. L. Ecklund, 1994: Wind profiler observations of Tropical Storm Flo at Saipan. *Wea. Forecasting,* **9,** 410–426.

Möller, J. D., and M. T. Montgomery, 1999: Vortex Rossby waves and hurricane intensification in a barotropic model. *J. Atmos. Sci.,* **56,** 1674–1687.

——, and ——, 2000: Tropical cyclone evolution via potential vorticity anomalies in a three-dimensional balance model. *J. Atmos. Sci.,* **57,** 3366–3387.

Montgomery, M. T., and R. J. Kallenbach, 1997: A theory for vortex Rossby-waves and its application to spiral bands and intensity changes in hurricanes. *Quart. J. Roy. Meteor. Soc.,* **123,** 435–465.

——, and J. Enagonio, 1998: Tropical cyclogenesis via convectively forced vortex Rossby waves in a three-dimensional quasigeostrophic model. *J. Atmos. Sci.,* **55,** 3176–3207.

Pandya, R. E., D. R. Durran, and M. L. Weisman, 2000: The influence of convective thermal forcing on the three-dimensional circulation around squall lines. *J. Atmos. Sci.,* **57,** 29–45.

Powell, M. D., 1990a: Boundary-layer structure and dynamics in outer hurricane rainbands. Part I: Mesoscale rainfall and kinematic structure. *Mon. Wea. Rev.,* **118,** 891–917.

——, 1990b: Boundary-layer structure and dynamics in outer hurricane rainbands. Part II: Downdraft modification and mixed layer recovery. *Mon. Wea. Rev.,* **118,** 918–938.

Raymond, D. J., 1992: Nonlinear balance and potential-vorticity thinking at large Rossby number. *Quart. J. Roy. Meteor. Soc.,* **118,** 987–1015.

——, and H. Jiang, 1990: A theory for long-lived mesoscale convective systems. *J. Atmos. Sci.,* **47,** 3067–3077.

Rotunno, R., J. B. Klemp, and M. L. Weisman, 1988: A theory for strong, long-lived squall lines. *J. Atmos. Sci.,* **45,** 463–485.

Samsury, C. E., and E. J. Zipser, 1995: Secondary wind maxima in hurricanes: Airflow and relationship to rainbands. *Mon. Wea. Rev.,* **123,** 3502–3517.

Schade, L. R., 1994: Comments on “Hurricane spiral bands.” *J. Atmos. Sci.,* **51,** 3543–3544.

Schubert, W. H., M. T. Montgomery, R. K. Taft, T. A. Guinn, S. R. Fulton, J. P. Kossin, and J. P. Edwards, 1999: Polygonal eyewalls, asymmetric eye contraction, and potential vorticity mixing in hurricanes. *J. Atmos. Sci.,* **56,** 1197–1223.

Smith, G. B., and M. T. Montgomery, 1995: Vortex axisymmetrisation: Dependence on azimuthal wavenumber or asymmetric radial structure changes. *Quart. J. Roy. Meteor. Soc.,* **121,** 1615–1650.

Smull, B. F., and R. A. Houze Jr., 1987: Rear inflow jets in squall lines with trailing stratiform precipitation. *Mon. Wea. Rev.,* **115,** 2869–2889.

Trier, S. B., W. C. Skamarock, and M. A. LeMone, 1997: Structure and evolution of the 22 February 1993 TOGA COARE squall line: Organization mechanisms inferred from numerical simulation. *J. Atmos. Sci.,* **54,** 386–407.

Wang, Y., 1999: A triply nested movable mesh tropical cyclone model with explicit cloud microphysics (TCM3). BMRC Research Rep. 74, Bureau of Meteorology Research Centre, Melbourne, Australia, 81 pp.

——, 2001: An explicit simulation of tropical cyclones with a triply nested movable mesh primitive equation model: TCM3. Part I: Model description and control experiment. *Mon. Wea. Rev.,* **129,** 1370–1394.

——, 2002: Vortex Rossby waves in a numerically simulated tropical cyclone. Part I: Overall structure, potential vorticity, and kinetic energy budgets. *J. Atmos. Sci.,* **59,** 1213–1238.

Webster, P. J., and G. L. Stephens, 1980: Tropical upper-tropospheric extended clouds: Inferences from Winter MONEX. *J. Atmos. Sci.,* **37,** 1521–1541.

Weisman, M. L., 1992: The role of convectively generated rear-inflow jets in the evolution of long-lived mesoconvective systems. *J. Atmos. Sci.,* **49,** 1826–1847.

——, and C. A. Davis, 1998: Mechanisms for the generation of mesoscale vortices with quasi-linear convective systems. *J. Atmos. Sci.,* **55,** 2603–2622.

Willoughby, H. E., J. A. Clos, and M. G. Shoreibah, 1982: Concentric eye walls, secondary wind maxima, and the evolution of the hurricane vortex. *J. Atmos. Sci.,* **39,** 395–411.

——, F. D. Marks Jr., and R. J. Feinberg, 1984: Stationary and moving convective bands in hurricanes. *J. Atmos. Sci.,* **41,** 505–514.

Yang, M.-J., and R. A. Houze Jr., 1995: Sensitivity of squall-line rear inflow to ice microphysics and environmental humidity. *Mon. Wea. Rev.,* **123,** 3175–3193.